Investigation of Airflow around Buildings using Large-Eddy Simulations for Unmanned Aircraft Systems Applications

Tyler R. Landua*, Rohit K. S. S. Vuppala†, and Kursat Kara‡
Oklahoma State University, Stillwater, Oklahoma 74078, United States

The ever-increasing demand for Unmanned Aircraft Systems (UAS) has led to the desire for integrating them into spaces in close proximity of humans like dense urban spaces, a reality previously thought of as inconceivable. One of the main concerns to be addressed before its widespread adoption is safety, especially in areas of operation adjacent to structures like buildings. This work investigates the effect of building geometries on the flow field in a simplified urban setup consisting of an isolated building to predict their potential impacts on UAS operations. Unanticipated wind gusts or turbulent flow conditions prevalent around various structures constitute a significant challenge for UAS operations in urban environments. We use Large-Eddy Simulation to better understand the unsteady and highly coherent turbulent flow structures produced by buildings in neutral atmospheric boundary layer flow. Furthermore, we also demonstrate a non-intrusive machine learning methodology to predict flow fields to augment safe wind-aware navigation systems for Unmanned Aerial Vehicles as a first step towards safely integrating UAS into existing aerial infrastructure.

I. Nomenclature

LES	=	Large-Eddy Simulation
$RANS$	=	Reynolds-Averaged Navier-Stokes
UAS	=	Unmanned Aircraft System
ML	=	Machine Learning
f	=	Coriolis parameter
ρ_0	=	density of dry air at surface
δ	=	Kronecker delta
ϵ	=	Levi-Civita symbol
$\prod$	=	Exner function
ψ	=	source/sink term
q_v	=	specific humidity
p	=	hydrostatic air pressure
R_d	=	specific gas constant for dry air
c_p	=	specific heat of dry air at a constant pressure
R_v	=	specific gas constant for water vapor
q_1	=	liquid mixing ratio
K_m	=	local SGS eddy diffusivity of momentum
K_h	=	local SGS eddy diffusivity of heat

II. Introduction

Unmanned aircraft represent a rapidly growing business sector. The Federal Aviation Administration (FAA) has recorded and continues to forecast steady growth in both hobby and commercial sectors of the UAS industry and expects the sector to double or triple in size by 2025 [1]. In light of this growth, integrating UAS into everyday life will be undeniably essential in the coming years. However, the integration of UAS into existing air travel and airspace

*Undergraduate Research Assistant, School of Mechanical and Aerospace Engineering, Student Member AIAA
†Graduate Research Assistant, School of Mechanical and Aerospace Engineering, Student Member AIAA
‡Assistant Professor, School of Mechanical and Aerospace Engineering, Senior Member AIAA

regulations is a daunting task, regarding both law and safety. Due to their relatively small size compared to common aircraft used for aviation, UAS are typically more vulnerable to flow conditions or rapid changes in their environment. According to the FAA and the National Center for Atmospheric Research (NCAR), wind and turbulence account for the vast majority of reported weather-related aviation accidents [2]. Considering their potential for accidents, UAS operations must be made as safe as possible.

The ability to recognize and adapt to avoid potentially dangerous regions for operation is one of the ways safety could be achieved. Understanding what makes an area safe or unsafe for a UAS comes down partly to understanding the region's airflow, turbulence, and potential obstacles. The detection and avoidance of physical objects is a subject of interest actively researched by both the industry and research community alike, yielding to recent adoption in civilian drones like DJI. These drones are equipped with obstacle avoidance systems using ultrasound and image data to detect and avoid physical hazards [3]. However, they do not have safeguards to prevent them from entering turbulent air regions that could rapidly destabilize a UAS, causing it to crash or veer off course. Airflow in urban areas is incredibly complex because of dense-packed structures like buildings. While a myriad of stimuli affect wind flow, the primary contribution to changes in flow in urban centers comes from buildings. Understanding these contributions is essential to estimate and predict how the flow is set up in urban centers and how building geometries affect the flow. Other systems could then augment UAS to approximate the potential turbulence created by various building geometries and change their flight path in real-time, avoiding potentially dangerous regions. Work done by Salazar et al. used a novel algorithm to generate wind field predictions and measurements from previous UAS flights to develop an estimation of wind conditions [4]. Still, this work did not investigate how the flow conditions they encountered were created. Combining building geometry effects with flow field predictions could lead to a new generation of drones that could recognize and avoid potentially dangerous regions utilizing the topology/terrain information like the location and geometry of the buildings around it.

In recent years, Computational Fluid Dynamics (CFD) approaches have been extensively used to analyze the wind flow around buildings without the need for extensive wind tunnel models to obtain solutions with adequate accuracy. While Reynolds-Averages Navier-Stokes (RANS) simulations can be used to solve for the flow fields, they do not accurately solve for their unsteady nature. However, Large-Eddy Simulations (LES) more accurately represent both the unsteady flow field and also closely match up with the averaged flow fields from wind tunnel testing results, though they are more computationally expensive [5]. When analyzing turbulent flow fields around three-dimensional bodies, researchers like Rodi et al. noted that the LES results were far more accurate than the RANS [6]. Especially in the case of a bluff body on a fixed surface, the RANS simulations over-predicted the flow separation behind the body. Both LES and RANS, however, are sensitive to the input parameters chosen. Much of the published work studying buildings using CFD has been to validate the approach by comparison to wind tunnel testing, natural ventilation inside buildings, or pollutant dispersion in street canyons [5] [7] [8] [9]. Little work has been done to study the effects of building geometry on wind flow with application to Unmanned Aircraft Systems.

This paper attempts to use Large-Eddy Simulations to investigate airflow over five simple yet common building geometries and identify potential hazardous regions of interest for safe UAS operation. These findings could then be generalized and modeled for operations near similar structures. The building shapes were considered in isolation to study the unique effects of each building, noting any similarities and differences. In addition, we investigated the impact of convection to determine if convection produces any effect on the flow fields at low altitudes.

III. Methodology

PALM is a turbulence-resolving, Large-Eddy Simulation solver for atmospheric and oceanic boundary-layer flows. The model is based on solving non-hydrostatic, filtered, incompressible Navier-Stokes equations in Boussinesq-approximated form on a Cartesian grid. Implicit separation of sub-grid scales and resolved scales is achieved by averaging the governing equations over discrete grid volumes as proposed by Schumann[8].

A. Governing Equations

The Navier-Stokes equations in the Boussinesq-approximated form are used as represented below. Brackets represent a horizontal domain average, and a subscript of zero indicates a surface value. The discretization implicitly filters variables in the equation, but the continuous form of the equations is used for convenience. The equations for conservation of mass, energy, and moisture filtered over a grid volume on a Cartesian grid are as follows.

$$\frac{\partial u_i}{\partial t} = \frac{-\partial u_i u_j}{\partial x_j} - \epsilon_{ijk} f_i u_k + \epsilon f_3 u_{g,j} - \frac{1}{\rho_0}\frac{\partial \pi *}{\partial x_i} + \frac{g(\theta_v - [\theta_v])}{[\theta_v]}\delta_{i3} - \frac{\partial}{\partial x_j}(u_i'' u_j'' - \frac{2}{3} e \delta_{ij}) \tag{1}$$

$$\frac{\partial u_j}{\partial x_j} = 0 \tag{2}$$

$$\frac{\partial \theta}{\partial t} = \frac{\partial u_j \theta}{\partial x_i} - \frac{\partial}{\partial x_i}(u_j'' \theta'') - \frac{Lv}{c_p \prod} \psi_{qv} \tag{3}$$

$$\frac{\partial q_v}{\partial t} = \frac{\partial u_j q_v}{\partial x_j} - \frac{\partial}{\partial x_j}(u_j'' q_v'') + \psi_{qv} \tag{4}$$

$$\frac{\partial s}{\partial t} = \frac{\partial u_j s}{\partial x_j} - \frac{\partial}{\partial x_j}(u_j'' s'') + \psi_s \tag{5}$$

where:

u_i = velocity components
x_i = a coordinate on the Cartesian grid
f = Coriolis parameter
ρ_0 = density of dry air at surface
δ = Kronecker delta
ϵ = Levi-Civita symbol
$\prod$ = Exner function
ψ = source/sink term
q_v = specific humidity

Furthermore, the sub-grid-scale turbulent kinetic energy can be written as:

$$e = \frac{1}{2} u_i'' u_j'' \tag{6}$$

And g is the gravitational acceleration. The potential temperature is defined as:

$$\theta = \frac{T}{\prod} \tag{7}$$

With the current absolute temperature T and Exner function:

$$\prod = (\frac{p}{p_0})^{\frac{R_d}{c_p}} \tag{8}$$

where:

p = hydrostatic air pressure
p_0 = 1000 hPa (a reference pressure)
R_d = specific gas constant for dry air
c_p = specific heat of dry air at a constant pressure

Thus, the virtual potential temperature is defined as:

$$\theta_v = \theta[1 + (\frac{R_v}{R_d} - 1) q_v - q_1] \tag{9}$$

where:

R_v = specific gas constant for water vapor
q_1 = liquid mixing ratio

B. Turbulence Closure

The following sub-grid-scale (SGS) model uses a 1.5 order closure based on modified version of Moeng and Wyngaard (1988) [10] and Saiki et al. (2000) [11]. The closure assumes that the energy transport by SGS eddies is proportional to the local gradients of the mean quantities.

$$\overline{u_i'' u_j''} - \frac{2}{3} e \delta_{ij} = -K_m \left(\frac{\partial u_i}{\partial x_j} + \frac{\partial u_j}{\partial x_i} \right) \tag{10}$$

$$\overline{u_i'' \theta''} = -K_h \frac{\partial \theta}{\partial x_i} \tag{11}$$

$$\overline{u_i'' q_v''} = -K_h \frac{\partial q_v}{\partial x_i} \tag{12}$$

$$\overline{u_i'' s''} = -K_h \frac{\partial s}{\partial x_i} \tag{13}$$

where:

K_m = local SGS eddy diffusivity of momentum
K_h = local SGS eddy diffusivity of heat

K_m and K_h are related to the SGS Turbulent Kinetic energy as follows:

$$K_m = c_m l \sqrt{e} \tag{14}$$

$$K_h = \left(1 + \frac{2l}{\Delta}\right) K_m \tag{15}$$

Where $c_m = 0.1$ is a model constant and

$$\Delta = min(1.8z, (\Delta x \Delta y \Delta z)^{\frac{1}{3}}) \tag{16}$$

The closure includes a prognostic equation for SGS Turbulent Kinetic Energy:

$$\frac{\partial e}{\partial t} = -u_j \frac{\partial e}{\partial x_j} - (\overline{u_i'' u_j''}) \frac{\partial u_i}{\partial x_j} + \frac{g}{\theta_{v,0}} \overline{u_3'' \theta_v''} - \frac{\partial}{\partial x_j} \left[\overline{u_j'' \left(e + \frac{p''}{\rho_0} \right)} \right] - \epsilon \tag{17}$$

Where the pressure term above is parametrized as:

$$\left[\overline{u_j'' \left(e + \frac{p''}{\rho_0} \right)} \right] = -2 K_m \frac{\partial e}{\partial x_j} \tag{18}$$

And ϵ is the SGS dissipation rate within a grid volume:

$$\epsilon = \left(0.19 + 0.74 \frac{l}{\Delta} \right) \frac{e^{\frac{3}{2}}}{l} \tag{19}$$

Note that θ_v depends on θ, q_v and q_1, the vertical SGS buoyancy flux depends on the respective SGS fluxes:

$$\overline{w'' \theta_v''} = K_1 \cdot \overline{w'' \theta''} + K_2 \cdot \overline{w'' q_v''} - \theta \cdot \overline{w'' q_1''} \tag{20}$$

where:

$$K_1 = 1 + \left(\frac{R_v}{R_d} - 1 \right) q_v - q_1 \tag{21}$$

$$K_2 = \left(\frac{R_v}{R_d} - 1 \right) \theta \tag{22}$$

$$\overline{w'' q_1''} = -K_h \frac{\partial q_1}{\partial z} \tag{23}$$

C. Boundary Conditions

PALM's obstacle code and LES model have been rigorously verified and tested in the past using wind tunnel comparisons conducted by Martinuzzi and Tropea [12]. While the LES model is well verified, the boundary conditions of each simulation are critical for the yielding of accurate results. According to work done by Blocken et al. [9], Franke et al. [13], and Chen and Zhai [14], boundary conditions should be cyclic on each side, inflow and outflow conditions for inlet and outlet and no-slip bottom condition. From work done by Letzel et al. [15], a top condition of zero gradient was used to ensure the boundary doesn't interfere with vertical flow resulting from convection effects. A drawing of the domain can be seen in Figure 1.

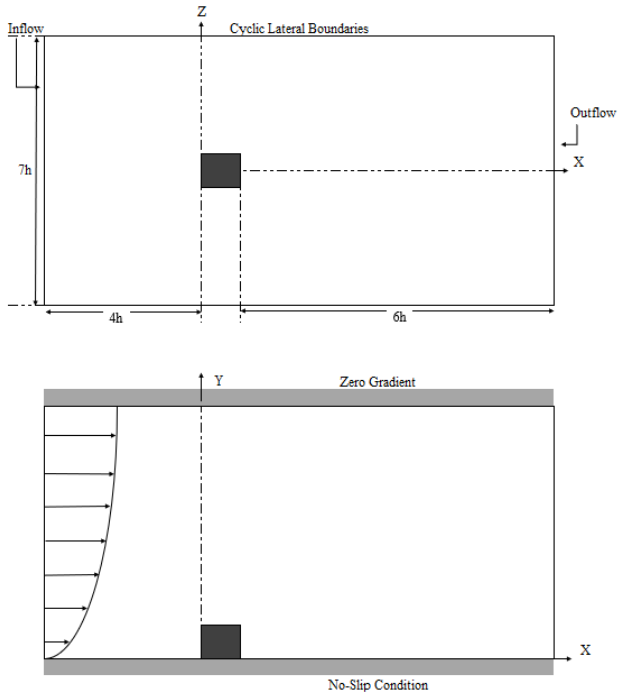

Fig. 1 Geometry of domain area with boundary conditions used. Note that this figure is not drawn to scale.

D. Validation

While CFD using Large-Eddy Simulation is an excellent tool for simulating and estimating the wind flow around buildings, it is still prone to error. This error may come from user error, as Hu mentioned in his proposed guidelines for CFD [16], or it could come from a limitation of the method and topography used in the simulation. For these reasons, Blocken et al. recommends validating CFD simulations against wind tunnel tests or other verified results [9]. Following the recommendation of Vardoulakis et al. [17] and Abohela et al. [18], the results of the rectangular building were compared to published results to verify the commonalities behind the flow field generated. Abohela et al. explained that the flow approaching the building should separate into four streams, two which flow around the building on each side, one which flows over the building, and one which is deviated downwards from the windward face into the ground. There should be a visible stagnation point which has the highest pressure on the windward segment at the location where the streams separate. A downward-flowing vortex should form in front of the building. The most notable structure is the horseshoe vortex which forms as the flow diverges around the building and converges again on the leeward side of the building [19].

The results of the rectangular flat-roofed building from our simulation follow closely with the flow phenomenon described by Vardoulakis et al. [17], Abohela et al. [18] and Seeta Ratnam and Vengadesan [19]. The stagnation point can clearly be seen in part (c) of Figure 2 as the high pressure region in front of the building. The division of the flow into four distinct paths can also clearly be seen in parts (a) and (b) of the same figure. Sub plot (a) shows the accelerating flow over the top of the building, and the standing vortex in front of the windward façade. Sub plot (b) shows the flow separate on each side of the building, recirculate behind the building and reattach in the leeward direction. In

our simulation, the leeward vortices reattached at 2.1h (h is the height of the building), which is congruent with Seeta Ratnam's and Vengadesan's [19] results of 2.2h. A small bubble of circulatory flow also occurred on the top of the building, per their results. On the leeward side of the building, two symmetrically located nodes, called the foci of separation, are visible in sub plot (b), and are formed from the spiral flow approaching them.

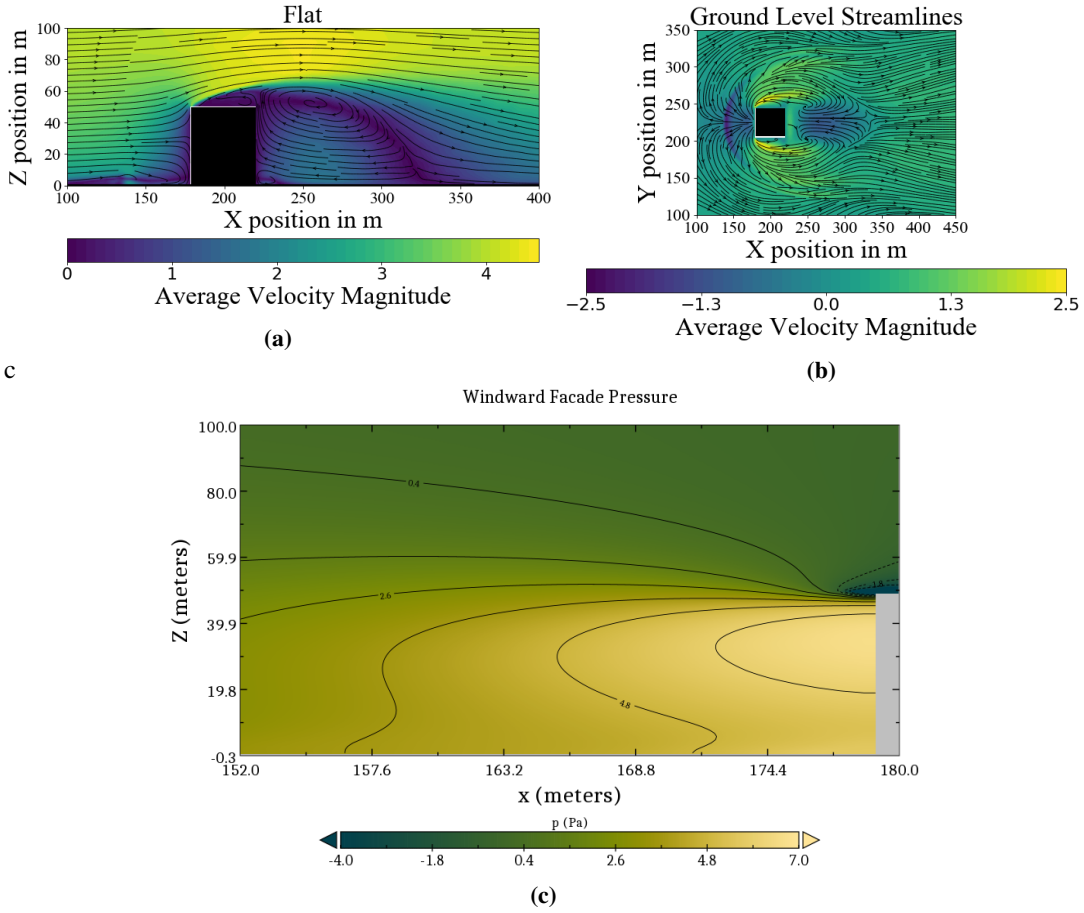

Fig. 2 Streamwise velocity streamlines and pressure gradient.

IV. Results

A. Simulation Setup

In order to study a variety of building configurations, five simple geometries were chosen and can be seen in Figure 3. These geometries were chosen since many building roofs in urban areas can be simplified as these shapes. Because PALM is limited to a Cartesian grid, complex surfaces are simplified with stair-like structures as can be seen in Figure 3. An arbitrary size of 40m x 40m x 49m was selected for the buildings. These sizes are arbitrary and could be in any other unit system. Each building was simulated with domain size of 576m x 448m x 320m. This domain was chosen to maintain an acceptable blockage ratio. According to Franke et al., blockage ratio should be at or less than 3% but should preferably be closer to 1.5% to maintain high quality results [13]. Table 1 shows the cross-sectional domain sizes and blockage ratios for each shape's simulation. Each case was driven by a parabolic inflow velocity following the equation

Table 1 Comparison of Case and Blockage Ratio.

Case	Building Frontal Area	Domain Cross-Section	Blockage Ratio
Pyramid	1580	1.14E+5	1.38%
Gabled	1580	1.14E+5	1.38%
Wedge	1960	1.14E+5	1.71%
Vaulted	1828	1.14E+5	1.60%
Flat	1960	1.14E+5	1.71%

below from Huang et al. [7], where U_H is wind speed at the height of the building model, and Z_H is the height of the model. Huang et al. also tested a log model to calculate inlet velocity distribution but discovered the difference in turbulence between these two equations is negligible. For our study, a maximum wind velocity, that is the velocity at the height of the model, was chosen to be 4m/s, which is the average wind velocity in Stillwater, Oklahoma, the location of Oklahoma State University.

$$\frac{U}{U_H} = \left(\frac{Z}{Z_H}\right)^{0.25} \tag{24}$$

Dry, adiabatic conditions were used so no moisture, humidity, or precipitation was considered. The simulation was run for two hours, with results being captured after the first hour had elapsed. Data points were collected and averaged every six seconds. According to the CFD guideline by Blocken et al. [9] and Chen and Zhai [14], the following requirements should be observed: scaled residuals must be between 10E-4 and 10E-6, mesh cells should be equidistant, details of dimension should be equal to or more than 1 m, and a stretching ratio less than 1.3 should be used if stretching is used. Our simulation took all of these into account as there is no stretching, the details of dimension are 1 m, and PALM's scaled residuals are less than 10E-4.

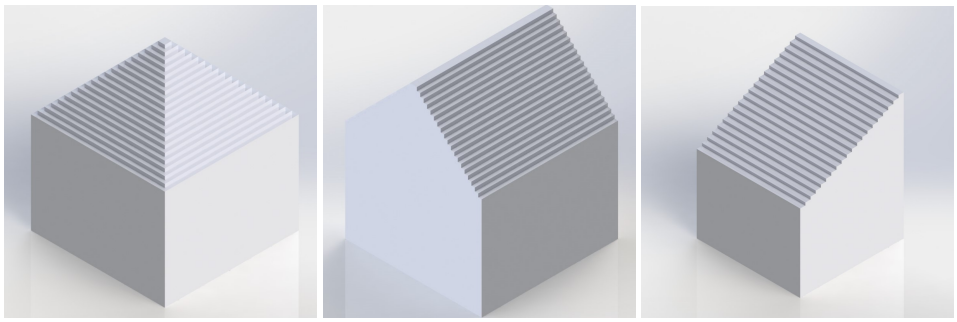

(a) Pyramid **(b) Gabled** **(c) Wedge**

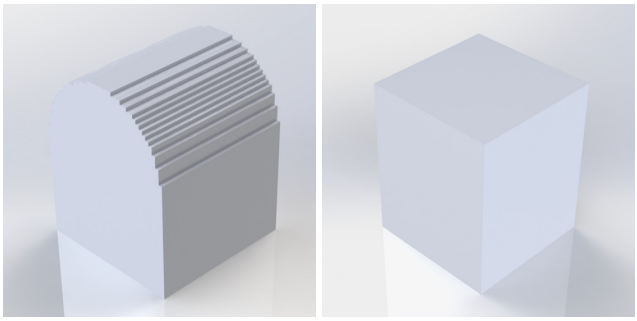

(d) Vaulted **(e) Flat**

Fig. 3 Building Geometries

Small UAS in an urban environment are sensitive to two factors that are the result of a building's presence in the flow field. Those two factors are changes in velocity and turbulent intensity around the building. Rapid velocity changes

present a challenge to small air vehicles because of control input lag. Consider a situation where a pilot or program controlling a UAS was unaware of a rapidly increasing velocity when the drone flew through this region. In a fraction of a second, the UAS could be shifted a far distance from where the controller believes the vehicle is, potentially resulting in an accident. Turbulent intensity holds similar consequences, with the flow field becoming violent in areas of high turbulent intensity caused by building geometry.

B. Flow Field Investigation

Beginning the investigation of the flow field, it is apparent from Figure 4 that the geometry of the building has a discernible impact on the flow field it generates. The velocities in these plots represent averages over the entire simulation time, with data being output every six seconds to create a high-fidelity average. Each plot represents the averages taken at a vertical slice through the domain whose X coordinate was 1H, 2H, and 3H behind the building respectively. Each slice was taken halfway through the domain in the Y direction. Using building height as the distance condition nondimensionalizes the distance, allowing these results to be universally compared.

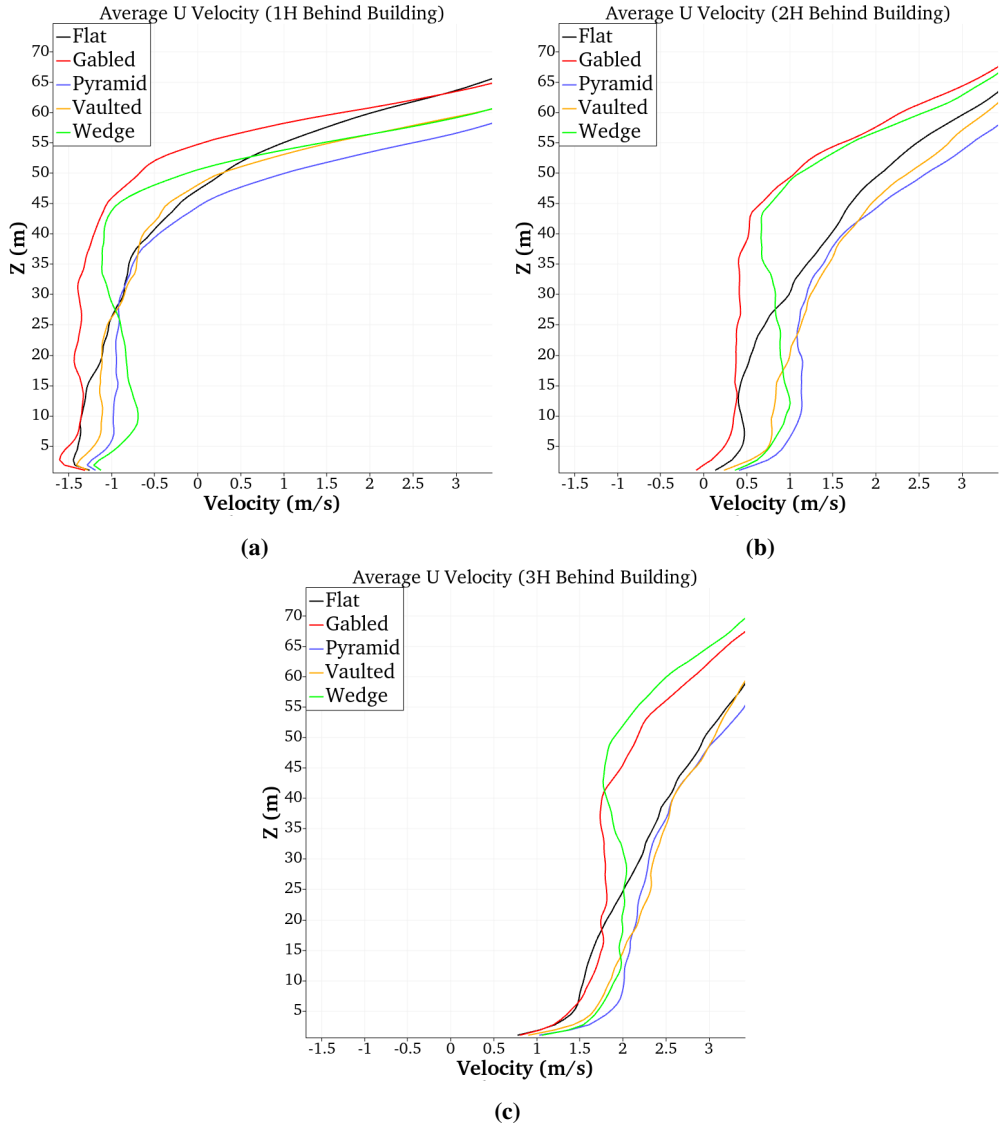

Fig. 4 Average U Velocities

Interestingly, the flat case almost serves as an average of each case, with its velocities coming in at the middle of the pack in 2H and 3H plots. It is apparent, however, that the sharp leading edge of the flat roof creates a short burst of

velocity over the top, as in subplot (a), the flat case has the highest velocity at the greatest height in the Z direction. As with each topography, a flow reversal can be seen behind the flat building at every height below the top of the building. This region represents the area of recirculating air, which can also be seen in subplot (b) of Figure 2, created by the upstream flow as it moves spirally towards the reattachment point.

Continuing with the gabled case, this topography, along with the wedge shape, projects accelerated flow into higher altitudes more than any other case. This can be seen easily as the average velocities at heights above the building remain high through each plot. In the 2H and 3H plots, the gabled building maintains high velocities at high Z values, while other configurations have these same velocities at lower Z values. For UAS applications, these results show that buildings with wedge or gabled shaped roofs pose a potential threat at altitudes far above the building itself, a threat which would not be detected by visual or sonar sensors.

The trend of projecting high velocity flow far above the building height is most apparent with the wedge case, as the maximum velocity is located at the highest Z height of all topographies tested. It is evident that the flow gradually gains energy over the wedge shape because at X distances closer to the building, the velocities are lower. This makes sense because the wedge shape ramps up in height along the entire width of the building, whereas the gabled building ramps up to the same height in half the building width, meaning a higher initial velocity, but a lower sustained velocity when looking at the same Z value.

Interestingly, even though the pyramidal shape shares some characteristics with the gabled shape, the pyramidal shape yielded the lowest average velocities at heights above the building than any other shape. It is clear, then, that the frontal area of the building plays a large role in the flow behind the building. Since the pyramidal shape has the lowest frontal area of the shapes tested, it follows that its velocities at each X value tested would be at lower Z values than the other shapes. Essentially, it is less efficient at changing flow field characteristics than the other cases. For UAS, this means that pyramidal buildings, or buildings with less wetted areas, pose less of a threat.

When analyzing the streamlines plot from Figure 5, it is clear that buildings create a significant area of circulating flow in the leeward direction. These areas, along with the standing vortex in front of the windward façade represent the areas with the highest turbulent intensity, meaning the air here is unstable. These areas represent potential threats and should be avoided.

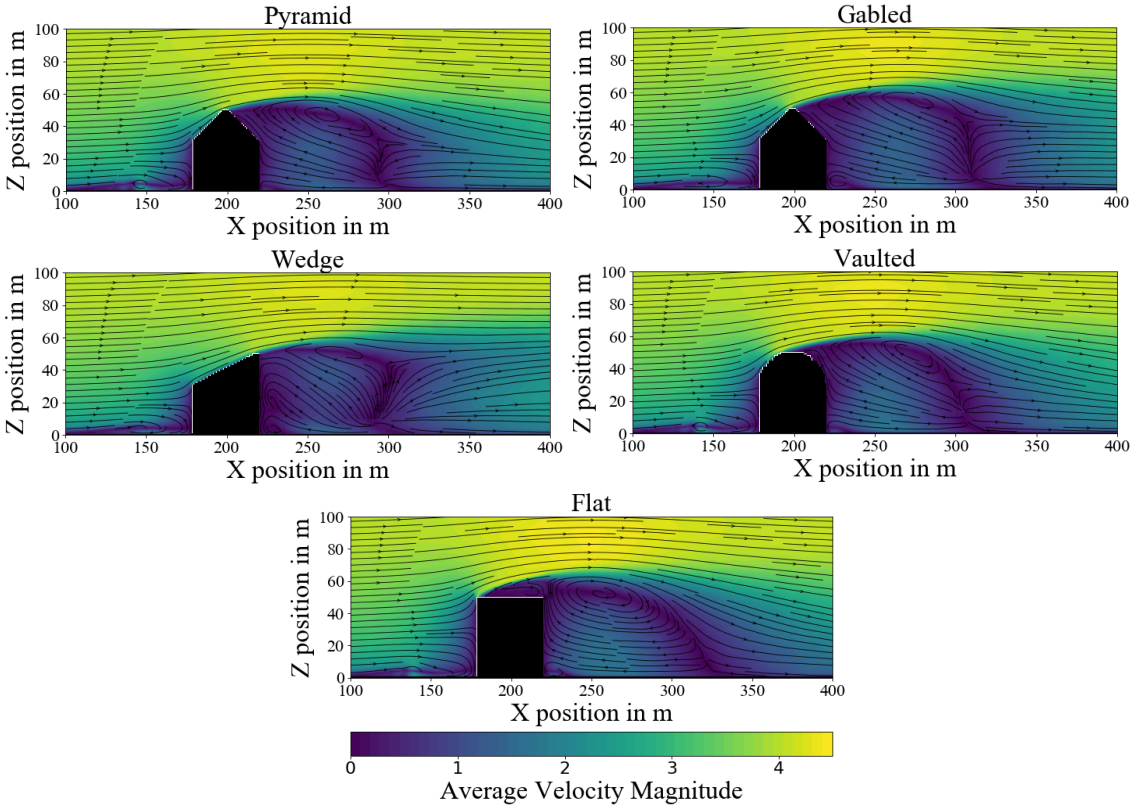

Fig. 5 Streamwise velocity streamlines through the vertical central plane.

C. Convective Effects

In an attempt to accurately simulate an urban environment, convection was considered during our simulations along with the non-convective cases already reviewed. It was found that for our case, convection did not play a large role in the development of the flow field. Figure 6 shows that at Z values between 0 m and 25 m, there is some discrepancy in the average U velocities between the convective and non-convective case, but above 25 m, the difference in flow is negligible. When looking at W velocities, the two cases follow the same trend throughout the simulation domain.

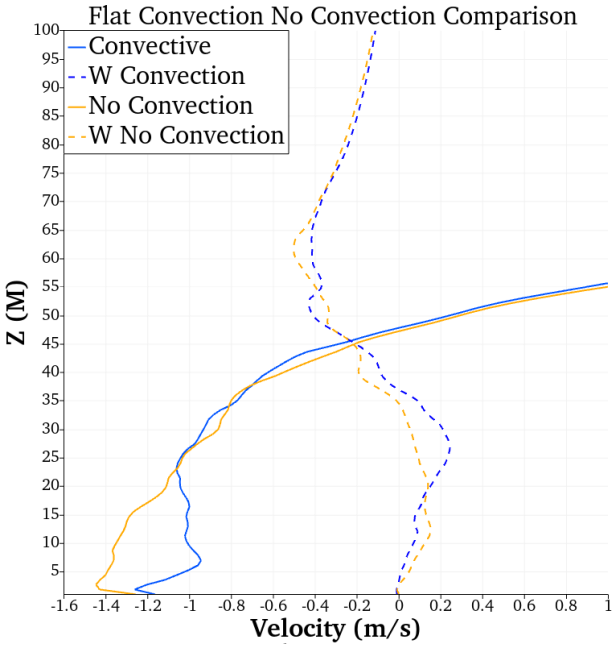

Fig. 6 Comparison of convective and non-convective simulations for the flat roof case.

These results are due primarily to the incoming velocity disturbing the creation of the convective structure. Figure 6 shows that while the inlet velocity is low, since the height is low at those points, the convective effects are noticeable in this small area. For the simulation as a whole, however, the convective effects are not noticeable. In the application of a small UAS, these results show that taking convective effects into account may actually provide more stable airflow near the surface, since the average U velocity under 25m is lower in the convective case than the non-convective case. More research is required to investigate this phenomenon specifically.

V. Machine Learning Predictions

Understanding the complex flow regions around buildings and urban canopies is the first step to creating a safe wind-aware navigation system for UAS in urban spaces. While high-fidelity numerical solutions like LES depict the highly complex flow structures accurately, they are computationally prohibitive to make flow field predictions. Hence, using Machine Learning to train on this high-fidelity data to make predictions is immensely helpful. Not only does it provide realistic wind data for testing and validating various algorithms like path-planning and control[20], it could also be used for real-time or close to real-time predictions where possible. We demonstrate the approach by utilizing the data from one of the building cases, precisely flat roof, to train the ML model and make flow field predictions.

A. Setup

After reaching a quasi-steady state, data is extracted from a smaller three-dimensional sub-domain region closer to the building to train the machine learning model as shown in Table 3. Snapshots of data were taken every second, training was done until 300 seconds, and predictions were made for 60 seconds. To further simplify the model only the x-component of velocity u is utilized for this work. Proper Orthogonal Decomposition is used on the 3D data and both modal coefficients and basis are calculated. We pick a threshold for relative information content as 80% giving us 35 modes as shown in Figure 7. The LSTM neural network is trained on these modes and predictions are made for

Parameter	Specification
Number of hidden layers	2
Number of neurons in each hidden layer	64
Activation function	tanh
Lookback time-window	20
Recurrent dropout	0.2
Neuron dropout	0.2
Loss function	MSE
Optimiser	ADAM
Training-testing ratio	5:1

Table 2 Neural Network details

future time-steps. The modes are then projected back to the 3D physical space using the previously calculated basis, for obtaining the flow field predictions. The neural network architecture used for the LSTM network is listed in Table 2. The approach followed here is very similar to the non-intrusive ROM-LSTM work in [21], for further details about the methodology, the reader is referred to the before-mentioned publication. The authors also note that similar methodology could also be adopted using Convolutional auto-Encoders instead of POD and using LSTM networks in tandem[22].

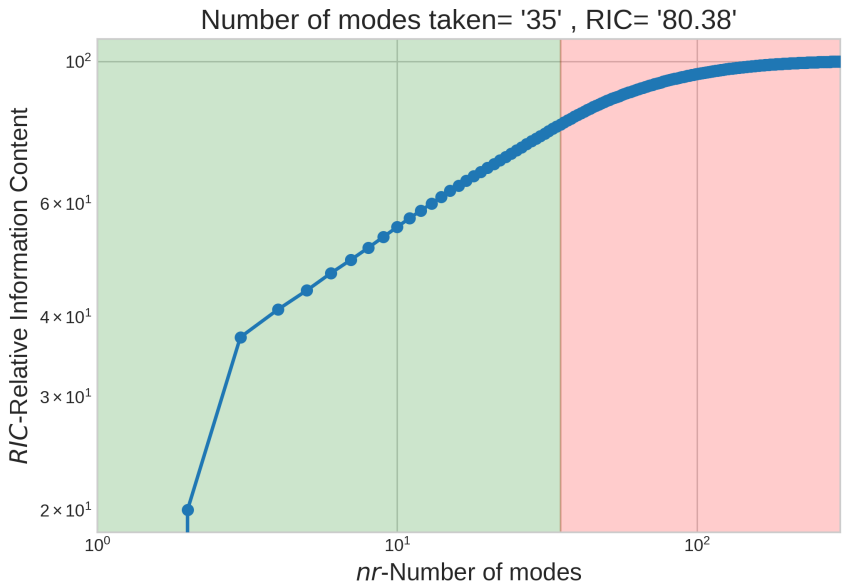

Fig. 7 Modes and their Relative Information Content; green-modes taken, red-modes neglected

Sub-Domain size for ML from center of the building	Specification
upstream (x-direction)	1.5H
downstream (x-direction)	3.5H
lateral (y-direction,both sides)	1.5H
above building (z-direction)	1H

Table 3 Sub-Domain used for ML training and predictions

B. Machine Learning Results

We see a good agreement between the predictions and the actual modes as shown in Figure 8. A contour plot in the xz direction in the center of domain is also plotted for comparison between the predicted u-velocity field and the POD reconstructed field from LES data in Figure 9. It could be noticed that there is a loss and mismatch between the finer structures in the contour plot. However, we have similar larger structures in the snapshots at 300, 330 and 360, closely resembling the reconstructed data it was trained on. As expected, the predictions are better at the 300th snapshot and deviate slowly as the number of the snapshot increases.

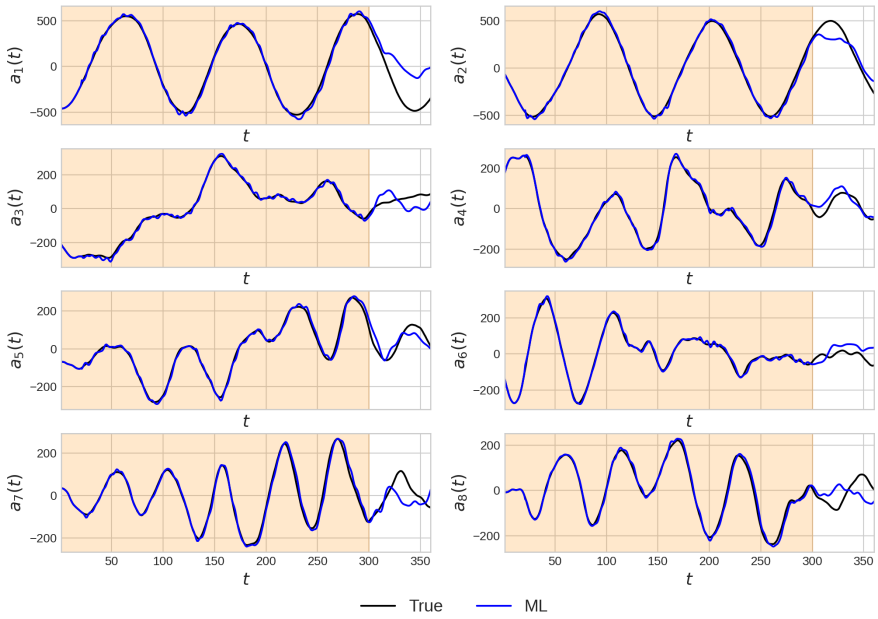

Fig. 8 Comparison between ML and true values for modes 1-8. Background colors: Tan/Orange - Training, White - Prediction

VI. Conclusions

Safety is paramount when considering the integration of UAS into existing aviation infrastructure, especially in dense urban spaces. Hence, ensuring the stability of UAS in the close proximity of buildings during navigation is essential to its safe operation. Understanding how flow fields are set up around buildings is a crucial step in various control and path-planning algorithms for developing a closely integrated wind-aware navigation system. Wind-aware UAS are better equipped to avoid potentially dangerous areas in the flow field by actively avoiding regions of gust or turbulence. Thus, in this paper, we investigated the effect of building geometry on the flow field in its vicinity using Large-Eddy Simulations. Each of these cases was then closely evaluated by analyzing the averaged flow field and comparing the region of turbulence created by the structures. We conclude that "Wedged" and "Gabled" roof structures pose the most significant threat to small UAS, as they create a larger region of turbulence, often at altitudes much greater than the highest surface of the building itself. For all these cases, it was noticed that there exists an area of turbulence and circulation up to a distance of 2.2H in the leeward direction, which could adversely affect safe UAS operation without adequate precautions. We also found that the data generated from these simulations could be used for making flow predictions using a non-intrusive Reduced Order Model-LSTM approach. Furthermore, the analysis from this work shows that building geometry has a significant impact on the flow field surrounding the building. At the heights tested, convective effects did not have a substantial effect on the flow. Further analysis of flow fields generated for different building geometries and other variations of flow conditions are required to create a more extensive database to augment the prediction of flow fields and safe navigation of UAS in urban spaces.

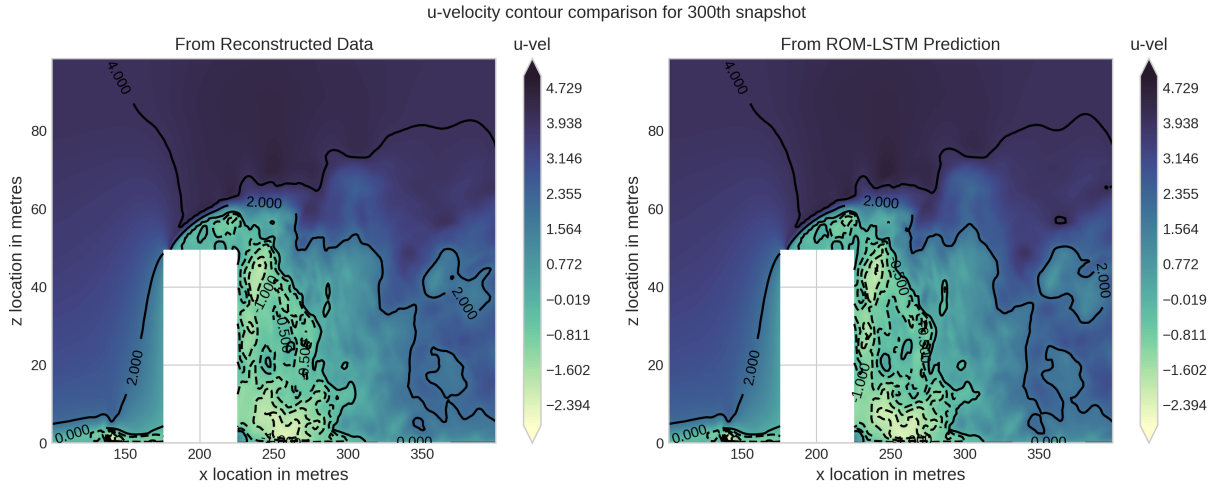

(a) u-velocity contour for xz plane in center of domain for 300th snapshot

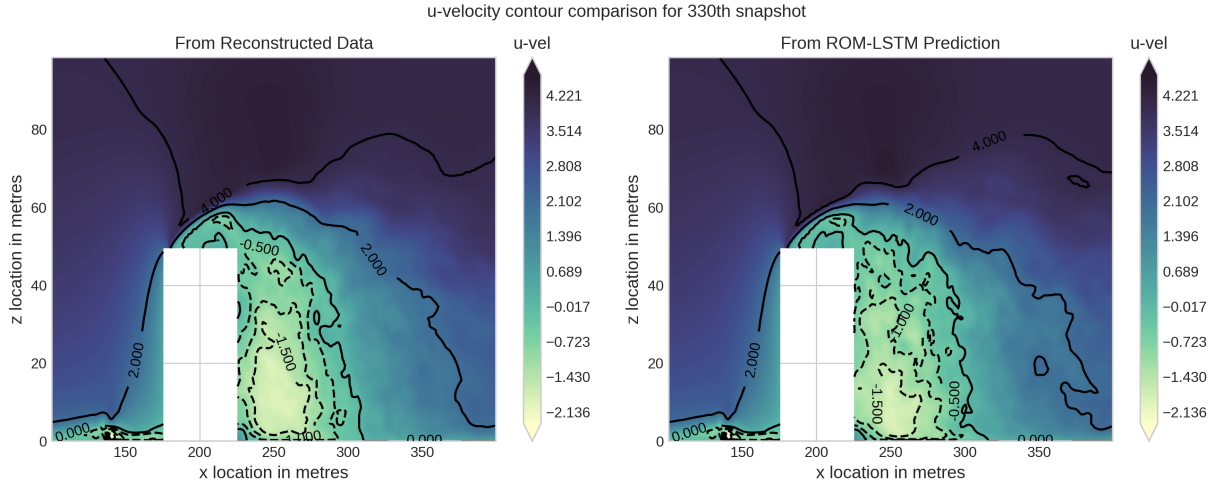

(b) u-velocity contour for xz plane in center of domain for 330th snapshot

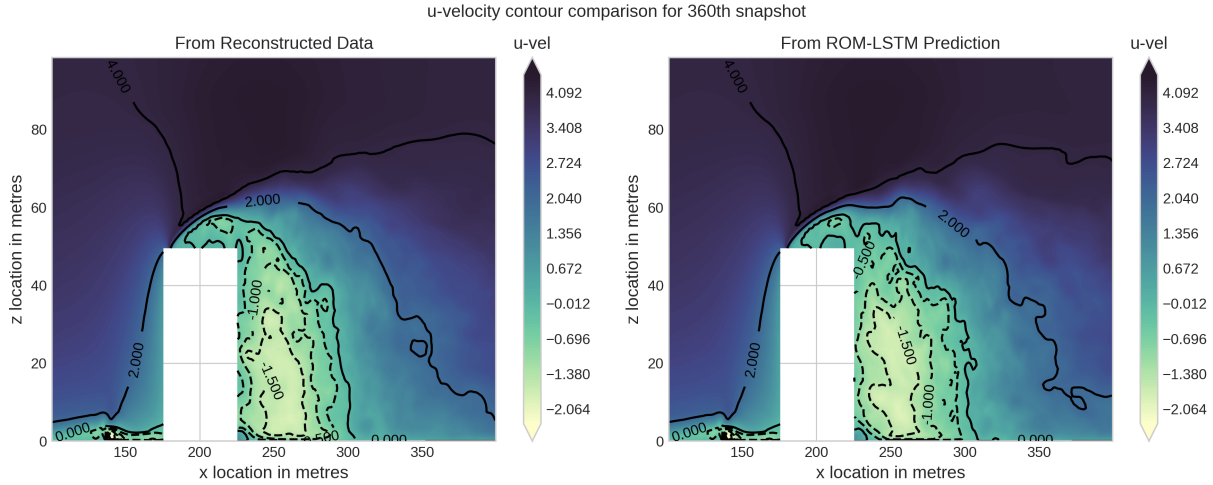

(c) u-velocity contour for xz plane in center of domain for 360th snapshot

Fig. 9 u-velocity contour for xz plane in center of domain

Acknowledgments

This material is based upon work supported by the National Science Foundation under Grant No. 1925147. Any opinions, findings, and conclusions or recommendations expressed in this material are those of the author(s) and do not necessarily reflect the views of the National Science Foundation. The first author is supported by Research Experiences for Undergraduates (REU) program. Some of the computing for this project was performed at the High-Performance Computing Center (HPCC) at Oklahoma State University supported in part through the National Science Foundation grant OAC-1531128. We would like to acknowledge high-performance computing support from Cheyenne[23] (doi:10.5065/D6RX99HX) provided by NCAR's Computational and Information Systems Laboratory, sponsored by the National Science Foundation.

References

[1] FAA, "FAA Aerospace Forecast Fiscal Years 2021–2041," 2020.

[2] Cornman, L. B., "Impact of Turbulence on Unmanned Aerial Vehicles," 2018.

[3] "Guidance - DJI," , 2021. URL `https://www.dji.com/guidance`.

[4] Rodriguez Salazar, L., Cobano, J. A., and Ollero, A., "Small UAS-Based Wind Feature Identification System Part 1: Integration and Validation," *Sensors*, Vol. 17, No. 1, 2017. https://doi.org/10.3390/s17010008, URL https://www.mdpi.com/1424-8220/17/1/8.

[5] Salim, S. M., Buccolieri, R., Chan, A., and Di Sabatino, S., "Numerical simulation of atmospheric pollutant dispersion in an urban street canyon: Comparison between RANS and LES," *Journal of Wind Engineering and Industrial Aerodynamics*, Vol. 99, No. 2, 2011, pp. 103–113. https://doi.org/https://doi.org/10.1016/j.jweia.2010.12.002, URL https://www.sciencedirect.com/science/article/pii/S0167610510001248.

[6] Rodi, W., "Comparison of LES and RANS calculations of the flow around bluff bodies," *Journal of Wind Engineering and Industrial Aerodynamics*, Vol. 69-71, 1997, pp. 55–75. https://doi.org/https://doi.org/10.1016/S0167-6105(97)00147-5, URL https://www.sciencedirect.com/science/article/pii/S0167610597001475, proceedings of the 3rd International Colloqium on Bluff Body Aerodynamics and Applications.

[7] Huang, S., Li, Q., and Xu, S., "Numerical evaluation of wind effects on a tall steel building by CFD," *Journal of Constructional Steel Research*, Vol. 63, No. 5, 2007, pp. 612–627. https://doi.org/https://doi.org/10.1016/j.jcsr.2006.06.033, URL https://www.sciencedirect.com/science/article/pii/S0143974X06001593.

[8] Schumann, U., "Subgrid scale model for finite difference simulations of turbulent flows in plane channels and annuli," *Journal of Computational Physics*, Vol. 18, No. 4, 1975, pp. 376–404. https://doi.org/https://doi.org/10.1016/0021-9991(75)90093-5, URL https://www.sciencedirect.com/science/article/pii/0021999175900935.

[9] Blocken, B., Stathopoulos, T., Carmeliet, J., and Hensen, J. L., "Application of computational fluid dynamics in building performance simulation for the outdoor environment: an overview," *Journal of building performance simulation*, Vol. 4, No. 2, 2011, pp. 157–184.

[10] Moeng CH, W. J., "Spectral analysis of large-eddy simulations of the convective boundary layeri," *Journal of Atmospheric Science*, Vol. 45, 1988, pp. 3573–3587. https://doi.org/https://doi.org/10.1016/0021-9991(75)90093-5.

[11] Saiki EM, S. P., Moeng CH, "Large-eddy simulation of the stably stratified planetary boundary layer," *Boundary Layer Meteorology*, 2000, pp. 1–30.

[12] Martinuzzi, R., and Tropea, C., "The Flow Around Surface-Mounted, Prismatic Obstacles Placed in a Fully Developed Channel Flow (Data Bank Contribution)," *Journal of Fluids Engineering*, Vol. 115, No. 1, 1993, pp. 85–92. https://doi.org/10.1115/1.2910118, URL https://doi.org/10.1115/1.2910118.

[13] Franke, J., Hellsten, A., Schlunzen, K. H., and Carissimo, B., "The COST 732 Best Practice Guideline for CFD simulation of flows in the urban environment: a summary," *International Journal of Environment and Pollution*, Vol. 44, No. 1-4, 2011, pp. 419–427.

[14] Chen, Q. Y., and Zhai, Z. J., "The use of Computational Fluid Dynamics tools for indoor environmental design," *Advanced building simulation*, Spon Press Oxfordshire, 2004.

[15] Letzel, M. O., Krane, M., and Raasch, S., "High resolution urban large-eddy simulation studies from street canyon to neighbourhood scale," *Atmospheric Environment*, Vol. 42, No. 38, 2008, pp. 8770–8784. https://doi.org/https://doi.org/10.1016/j.atmosenv.2008.08.001, URL https://www.sciencedirect.com/science/article/pii/S1352231008007036.

[16] Hu, C.-H. H., "Proposed guidelines of using CFD and the validity of the CFD models in the numerical simulations of wind environments around buildings," Ph.D. thesis, Heriot-Watt University, 2003.

[17] Vardoulakis, S., Dimitrova, R., Richards, K., Hamlyn, D., Camilleri, G., Weeks, M., Sini, J.-F., Britter, R., Borrego, C., Schatzmann, M., et al., "Numerical model inter-comparison for wind flow and turbulence around single-block buildings," *Environmental Modeling & Assessment*, Vol. 16, No. 2, 2011, pp. 169–181.

[18] Abohela, I., Hamza, N., and Dudek, S., "Effect of roof shape, wind direction, building height and urban configuration on the energy yield and positioning of roof mounted wind turbines," *Renewable Energy*, Vol. 50, 2013, pp. 1106–1118. https://doi.org/https://doi.org/10.1016/j.renene.2012.08.068, URL https://www.sciencedirect.com/science/article/pii/S0960148112005381.

[19] Ratnam, G. S., and Vengadesan, S., "Performance of two equation turbulence models for prediction of flow and heat transfer over a wall mounted cube," *International Journal of Heat and Mass Transfer*, Vol. 51, No. 11-12, 2008, pp. 2834–2846.

[20] Tabassum, A., Vuppala, R. K., Bai, H., and Kara, K., "Variance Reduction of Quadcopter Trajectory Tracking under Stochastic Wind Disturbances," *arXiv preprint arXiv:2104.10266*, 2021.

[21] Vuppala, R. K., and Kara, K., "A Novel Approach in Realistic Wind Data Generation for The Safe Operation of Small Unmanned Aerial Systems in Urban Environment," *AIAA AVIATION 2021 FORUM*, 2021, p. 2505.

[22] Vuppala, R. K. S. S., and Kara, K., "Realistic Wind Data Generation for Small Unmanned Air Systems in Urban Environment using Convolutional Autoencoders," *Bulletin of the American Physical Society*, 2021.

[23] Computational, and Laboratory, I. S., "Cheyenne: HPE/SGI ICE XA System (University Community Computing)," , 2017.